

New evidence for the ubiquity of prominent polar dust emission in AGN on tens of parsec scales

D. Asmus¹*

¹*Department of Physics & Astronomy, University of Southampton, Hampshire SO17 1BJ, Southampton, United Kingdom*

12 August 2019

ABSTRACT

The key ingredient of active galactic nuclei (AGN) unification, the dusty obscuring torus was so far held responsible for the observed mid-infrared (MIR) emission of AGN. However, the best studied objects with VLTI/MIDI show that instead a polar dusty wind is dominating these wavelengths, leaving little room for a torus contribution. But is this wind an ubiquitous part of the AGN? To test this, we conducted a straightforward detection experiment, using the upgraded VLT/VISIR for deep subarcsecond resolution MIR imaging of a sample of nine [O IV]-bright, obscured AGN, all of which were predicted to have detectable polar emission. Indeed, the new data reveal such emission in all objects but one. We further estimate lower limits on the extent of the polar dust and show that the polar dust emission is dominating the total MIR emission of the AGN. These findings support the scenario that polar dust is not only ubiquitous in AGN but also an integral part of its structure, processing a significant part of the primary radiation. The polar dust has to be optically thin on average, which explains, e.g., the small dispersion in the observed mid-infrared–X-ray luminosity correlation. At the same time, it has to be taken into account when deriving covering factors of obscuring material from mid-infrared to bolometric luminosity ratios. Finally, we find a new tentative trend of increasing MIR emission size with increasing Eddington ratio.

Key words: galaxies: active – galaxies: Seyfert – infrared: galaxies

1 INTRODUCTION

It seems beyond doubt that active galactic nuclei (AGN) contain large amounts of dust which is heated by the accretion onto the supermassive black hole, leading to copious amounts of mid-infrared (MIR) emission, which in fact contains roughly half of the total power output of these systems. It also is established that the innermost region of AGN is highly obscured for a significant fraction of their sky as originally inferred the presence of scattered light from the central region, visible in polarized light, and the presence of collimated ionization cones (Antonucci 1993). This led to the common assumption that this obscuring material is distributed into a torus-like structure, which then would be also main MIR emitter, (e.g., Nenkova et al. 2008; see Netzer 2015 and Almeida & Ricci 2017 for recent reviews). However, this could never been directly shown, and there is growing evidence to the contrary. Namely, the highest angular resolution MIR observations available obtained with VLTI/MIDI interferometry show that most of the MIR emission is coming from a polar extended component (Hönig et al. 2012, 2013; Tristram et al. 2014; López-Gonzaga et al. 2014, 2016; Leftley et al. 2018). It turned out that this polar component can also be resolved with subarcsecond resolution single dish imaging in the

MIR and, thus, extends up to scales of tens to hundreds of parsec (e.g., Bock et al. 2000; Radomski et al. 2003; Packham et al. 2005; Asmus et al. 2014; Asmus, Hönig & Gandhi 2016; hereafter A16). Recently, it has been detected on even larger scales (and longer wavelengths; Fuller et al. 2019). This means that this polar dust is present at similar scales as the narrow-line emitting region (NLR) of the AGN, and is probably forming a hollow cone-like structure surrounding the NLR. In addition to the polar extended component, the VLTI/MIDI observations found a second, more compact component, which could be resolved into a equatorial disk in the objects with the best u,v coverage. The two components can be interpreted as a dusty hollow cone, or hyperboloid, and a dusty thin disk as extension of the outer accretion disk, respectively. Such a dust geometry can indeed successfully reproduce many observed infrared properties of the Seyferts (Hönig & Kishimoto 2017). It also allowed us to explain all observed infrared features of the intrinsically best resolved AGN, in the Circinus galaxy at once (Stalevski, Asmus & Tristram 2017; Vollmer et al. 2018; Stalevski, Tristram & Asmus 2019). On the other hand, no match could be found with the classical clumpy torus model for Circinus. In particular the observed morphology and interferometric visibilities could not reproduced, even after adding dust in the polar region.

Dynamically, Hönig et al. (2012) interpreted this polar dust structure as a dusty wind driven by the radiation of the accretion

* E-mail: d.asmus@soton.ac.uk

disk. In that case, the actual obscurer could be a much more compact and quite hot structure like a puffed up outer accretion disk (see also Baskin & Laor 2018), as also assumed to occur in disks around forming stars, or a combination of such a puff-up and the base of the polar wind (see also Elitzur & Shlosman 2006 and Wada 2012 for similar ideas). In the best fitting model for Circinus by Stalevski, Tristram & Asmus (2019), the base of the polar dusty wind is indeed optically thick and significantly contributes to the obscuration. This raises the possibility that the obscuration along our line of sight to some Seyferts is dominated by the polar dust but we expect this to be the case only for a small fraction owing the polar dust component covering only $\sim 10\%$ of the sky as seen by the central source. Then, on scales larger than a few parsec, the polar dusty wind becomes on average optically thin as it is required by the fact that we have a relatively clear line of sight towards the ionization cone.

From the physical side, the above scenario is also well motivated as radiation pressure has been suspected as major driver for the geometrical thickness of the obscuring material for a long time (Pier & Krolik 1992; Konigl & Kartje 1994; Elvis 2000; Roth et al. 2012). In fact, polar dusty winds are now also successfully produced by hydrodynamical models (Chan & Krolik 2016; Wada, Schartmann & Meijerink 2016; Williamson, Hönig & Venanzi 2019).

If this new scenario of the dust structure would hold true for the AGN population in general, it could have fundamental impact on the current AGN research field, which based many results on the presence of a infrared-prominent clumpy dust torus like, e.g., the determination of covering factors of obscuring material (e.g., Ramos Almeida et al. 2009, 2011; Alonso-Herrero et al. 2011). Therefore, it is crucial to test how ubiquitous this polar dust phenomenon is. One of the major caveats of the scenario is that it is based on the findings for relatively few objects so far.

A16 made the first statistical investigation of the polar dust phenomenon by looking at all archival subarcsecond resolution MIR images of those AGN which, on the one hand, show no nuclear starburst, and, on the other hand, are at least moderately powerful, i.e. no LINERs. Only a small fraction of the sources (21 of 149) showed robust evidence for extended emission. This low detection rate was explained by the combination of several factors. First, only in sufficiently inclined systems, i.e. obscured AGN, one expects to be able to clearly detect the polar emission. Second, the objects have to be close and powerful enough, so that we can actually resolve the polar emission with direct imaging. And finally, most of the available data are relatively shallow, barely enough to detect the nuclear component in many cases, and thus insufficient to robustly detect extended emission. So the results so far are consistent with every AGN having strong polar dust emission but its low detection rate leaves a lot of room for ambiguity.

To further test the ubiquity of polar dust emission, we have now performed a detection experiment by utilizing a prediction that is made in A16. Namely, it was found that the amount of extended MIR emission correlates with the [OIV] $25.89\mu\text{m}$ emission line flux. This line originates from the ionization cone and, thus, comparable scales than the polar MIR emission. Thanks to in general negligible obscuration and resulting isotropy, the [OIV] $25.89\mu\text{m}$ line has been found to be one of the best intrinsic indicators for the AGN bolometric luminosity (Meléndez et al. 2008). Therefore, it is expected that objects with higher [OIV] fluxes have either more powerful AGN, and thus probably larger cones, or are simply more nearby. Either way, a higher [OIV] flux implies a larger apparent size on the sky. This explains why all objects above a certain thresh-

Table 1. Selected sample for new VISIR observations.

Object	Opt. class	D [Mpc]	$\log F$ ([OIV]) [erg/cm/s ²]	Ref.
(1)	(2)	(3)	(4)	(5)
3C 321	2.0	460.0	-12.1	1
IC 4518W	2.0	76.1	-12.1	2
Mrk 573	2.0	73.1	-12.1	3
NGC 1365	1.8	17.9	-11.8	4
NGC 2110	2.0	35.9	-12.3	5
NGC 5135	2.0	66.0	-12.2	6
NGC 5506	1.9	31.6	-11.7	4
NGC 5643	2.0	20.9	-12.1	4
NGC 7582	1.8	23.0	-11.6	6

– *Notes:* (1), (2), and (3) object name, optical class, and distance (D) from Asmus et al. (2014); (4) and (5) observed [OIV] flux, $F([\text{OIV}])$, from *Spitzer*/IRS and corresponding reference: 1: Dicken et al. (2014); 2: Pereira-Santaella et al. (2010); 3: Sturm et al. (2002); 4: Diamond-Stanic, Rieke & Rigby (2009); 5: Weaver et al. (2010); 6: Tommasin et al. (2010);

old in [OIV] line flux, i.e., $F([\text{OIV}]) \geq 6 \cdot 10^{-13} \text{ erg/s/cm}^{-2}$, could be resolved and show polar MIR emission in the A16 sample. The value of this threshold depends on our instrumentation. Conclusively, the prediction is that all AGN with an [OIV] flux larger than this threshold should have polar MIR emission detectable with 8 meter class telescopes.

2 SAMPLE SELECTION

To test the above prediction, we searched the NASA/IPAC Extragalactic Database (NED¹) for all galaxies with available [OIV] measurements taken either with the *ISO* or *Spitzer* satellite (Kessler et al. 1996; Werner et al. 2004) We found 596 local galaxies ($z \leq 0.1$), of which 32 have [OIV] fluxes above the empirical polar dust detection threshold from A16 of $6 \cdot 10^{-13} \text{ erg/s/cm}^{-2}$ ($\log F([\text{OIV}])/[\text{erg/s}] \geq -12.2$). From those, we select only those 25 objects that harbour obscured AGN because for those the probability of being highly-inclined with respect to our line of sight is higher. For these objects, the polar dust cones should lead to a clearly elongated MIR structure in the observations. Furthermore, we exclude Mrk 463E because this is a starbursting host in the merging process, leading to confusing MIR emission, and the very nearby starburst, but uncertain AGN, in NGC 253 (e.g., Günthardt et al. 2015). Of the remaining 23, 12 have already verified polar MIR emission. This leaves 11 obscured AGN of which 8 are visible from Paranal. Their basic properties including the [OIV] fluxes are listed in Table 1.

The prediction is that all of these 8 should exhibit detectable polar MIR emission. To the sample, we further added another source, NGC 2110, because previous MIR imaging indicated that its nucleus is possibly extended (Asmus et al. 2014).

¹ <http://ned.ipac.caltech.edu/>

3 OBSERVATIONS

We observed the 9 selected obscured AGN with the Very Large Telescope (VLT) mounted Spectrometer and Imager for the Mid-infrared (VISIR; Lagage et al. 2004) after its upgrade (Käufl et al. 2015; Kerber et al. 2016) in service mode between May 2017 and July 2018 (programme 099.B-0044; PI: Asmus). Images were recorded in the two filters B12.4 ($12.47 \pm 0.5 \mu\text{m}$) and Q1 ($17.65 \pm 0.44 \mu\text{m}$) with standard chopping and perpendicular nodding using a chop/nod throw of $8''$ and an on-source exposure times of 30 min each. For 3C 321 and NGC 5506, no successful observation in B12.4 could be made before the termination of the programme. To allow for accurate point-spread-function (PSF) subtraction, a nearby (within 10°) calibrator star taken from Cohen et al. (1999) was observed either directly before or after with 2 min on-source exposure times per filter. The data were custom reduced and analysed with an in-house developed, python-based pipeline. Details of the observations and the individual measurements are listed in Table 2.

4 RESULTS & DISCUSSION

4.1 Presence of extended MIR emission

The VISIR images obtained for all sources are shown in Fig. 1. All nuclei were clearly detected, whereas for NGC 5135 and NGC 7582 also the known kiloparsec-scale circum-nuclear starburst rings are partly visible (see, e.g., Asmus et al. 2014 for discussion). To roughly characterise the nuclear structures, we measure the total flux, extension and position angle (PA) of the nuclear emission with Gaussian fitting. The resulting values are listed in Table 2 in comparison to the similarly obtained values of the PSF reference stars.

All nuclei, except those of NGC 5135 and NGC 7582, show Gaussian-fit major axis full width half maximum (FWHM) values that are 10 to 20% larger than those of the PSF references (median: 12%). In general, the level of resolvedness is 10% larger in the B12.4 filter compared to that in the Q1 filter. This is expected given the $\sim 30\%$ better angular resolution ($0.34''$ versus $0.45''$), and the ~ 3 times better sensitivity in B12.4 compared to Q1 (7.5 mJy versus 24 mJy, respectively, for 10σ in one hour on-source integration time). In our case, these two advantages seem to outweigh the expected larger extent of the MIR emission at longer wavelengths as a result of the centrally peaked temperature distribution of the dust. The nucleus of NGC 1365 is here the only exception with the resolvedness being larger in Q1 compared to B12.4 (23% versus 16%).

In order to better trace the extended emission, we subtract the unresolved core emission from each nucleus as shown in Fig. 2. In this figure, the core is actually over-subtracted (PSF peak scaled to total peak emission) to maximise the visibility of the extended emission. Here, and in the following analysis, we prefer the B12.4 images over Q1 ones (whenever both are available), owing to better angular resolution and sensitivity. After the core subtraction, all objects, except NGC 5135, show clearly extended emission. Even in NGC 5135 extended emission might be present as indicated by the low significance structures in the image ($\sim 3\sigma$). Interestingly, the nuclear region of NGC 5135 remained undetected also in recent high resolution ALMA observations tracing cold dust and molecular gas (Cao et al. 2018), implying that the AGN in this object might have used up most of its fuel. In that case, the bright [O IV] emission might be coming predominantly from the kiloparsec scales, i.e. the outer NLR, as a relict of its more active past.

We verify the robustness of the extended emission detection

by using the observatory provided standard stars observed in the same nights instead of our own PSF calibrators. Owing to the PSF not being very stable in ground-based MIR observations and the observations of those standard stars being further away in time and/or sky direction, they are less suitable as PSF references. Nevertheless, we obtain similar extended structures after PSF subtraction in all cases but NGC 7582. In the latter case, the PSF of observatory standard is clearly more elongated than our own and thus its subtraction leads to significant negative residuals hiding any real structure. Therefore, we conclude from this check that the detection of extended emission is indeed robust.

4.2 Alignment of extended MIR emission

To verify if the extended MIR emission is consistent with coming from the polar region of the AGN, we compare the MIR PA estimated from the Gaussian fits to the system axis (SA) PAs collected from the literature. The corresponding MIR PAs and SA PAs are listed in Table 3. The latter are based on PAs measured from [O III] cones, maser disks, outflows and/or polarized broad-line emission and were collected in A16 already. We refer the reader to that work for more details on this.

Fig. 2 shows the SA PAs over-plotted on top of the MIR emission. Indeed, both seem to align reasonably well. Quantitatively, the MIR PA and SA PA agree to within 23° median (12° standard deviation) with the largest difference of $\sim 39^\circ$ for Mrk 573. Note that even for an apparent misalignment of $\sim 45^\circ$, the MIR emission can still be consistent with a polar origin as shown for the Circinus AGN, where the angular difference between SA and MIR seems to be caused by the accretion disk being tilted towards one side of the polar cone (Stalevski, Asmus & Tristram 2017).

At the same time, the MIR emission does not align with host structure PAs (taken as well from A16 and listed in Table 3). Here, the median angular difference is 62° with a standard deviation of 26° . Clearly, the preferred origin of the extended MIR emission is the polar region of AGN rather than host-related structures, verifying the findings of A16 (see also Fischer et al. 2013).

Finally, we combine the here presented sample with the objects from A16 and show the updated distribution of MIR–SA PA difference in Fig. 3. Adding the new sources does not change the median alignment between the MIR and SA PAs (19°), while the standard deviation slightly decreases from 27° to 23° .

The above results leave little doubt on a polar origin for the extended MIR emission, while its high detection rate among our test sample verifies our hypothesis that polar dust emission on tens to hundreds of parsec scale might be an ubiquitous feature of the AGN structure. One has to keep in mind though that this hypothesis could only be tested for AGN in the Seyfert regime with a bright NLR, owing to the [O IV] flux selection. Given the likely origin of the polar dust as a wind/outflow, it is entirely possible, and probably even to be expected, that the presence and prominence of it will depend on the AGN fundamental parameters like the bolometric luminosity and Eddington ratio. In order to do that (see Sect. 4.5) we first need to constrain the strength and extent of the polar dust emission.

4.3 Dominance of polar dust emission

To understand how relevant the polar dust emission is for the energy budget of the AGN, we derive lower limits on its relative contribution, $R_{\text{AGN}}^{\text{pol}}$, towards the total MIR emission of the AGN, which

Table 2. Observations

Object	Filter	Date [yyyy-mm-dd]	Cal. name	Sensit. [mJy $10\sigma/1h$]	Cal. Maj. [as]	Cal. Min. [as]	Cal. PA [$^\circ$]	Sci. Maj. [as]	Sci. Min. [as]	Sci. PA [$^\circ$]	Gauss flux [mJy]
(1)	(2)	(3)	(4)	(5)	(6)	(7)	(8)	(9)	(10)	(11)	(12)
3C 321	Q1	2018-07-10	HD141992	25.5	0.49	0.45	4	1.03	0.68	99	154
IC 4518W	B12.4	2018-04-23	HD136422	8.6	0.34	0.33	151	0.41	0.36	17	210
IC 4518W	Q1	2017-07-28	HD136422	27.9	0.49	0.47	166	0.55	0.50	0	366
Mrk 573	B12.4	2017-08-08	HD10380	5.2	0.36	0.32	6	0.42	0.38	169	275
Mrk 573	Q1	2017-08-06	HD10380	22.8	0.45	0.43	0	0.50	0.45	157	461
NGC 1365	B12.4	2017-08-30	HD26967	5.9	0.37	0.36	63	0.43	0.38	102	434
NGC 1365	Q1	2017-09-12	HD26967	20.5	0.53	0.53	107	0.65	0.57	105	692
NGC 2110	B12.4	2017-10-01	HD39853	5.1	0.37	0.37	54	0.58	0.53	17	361
NGC 2110	Q1	2017-09-27	HD39853	26.0	0.46	0.44	17	0.47	0.46	165	569
NGC 5135	B12.4	2018-07-23	HD123139	10.4	0.42	0.39	6	0.43	0.38	1	123
NGC 5135	Q1	2018-07-09	HD123139	21.0	0.46	0.45	7	0.48	0.43	20	201
NGC 5506	Q1	2018-07-08	HD124294	26.1	0.45	0.45	19	0.49	0.46	24	1923
NGC 5643	B12.4	2018-06-12	HD136422	8.3	0.34	0.33	5	0.41	0.39	67	265
NGC 5643	Q1	2017-07-26	HD136422	25.0	0.46	0.44	8	0.50	0.49	55	855
NGC 7582	B12.4	2017-09-04	HD22261	9.0	0.38	0.35	130	0.38	0.38	82	494
NGC 7582	Q1	2017-06-21	HD22261	25.3	0.49	0.46	144	0.50	0.47	125	552

– *Notes:* (1) object name; (2) instrument filter B12.4 ($12.47 \pm 0.5 \mu\text{m}$) and Q1 ($17.65 \pm 0.44 \mu\text{m}$); (3) date of the observation; (4) name of the calibrator star used as flux and PSF reference; (5) derived sensitivity from the calibrator observation following the definition used by ESO (VISIR manual); (6), (7) and (8) major and minor axis FWHM and corresponding position angle of the PSF derived from Gaussian fitting of the calibrator star; (9), (10) and (11) major and minor axis FWHM and corresponding position angle of the PSF derived from Gaussian fitting of the science target; (12) derived flux density from the Gaussian fitting of the science target; the associated uncertainty of this measurement is dominated by the systematic uncertainty on the flux of the calibrator star and is 10%.

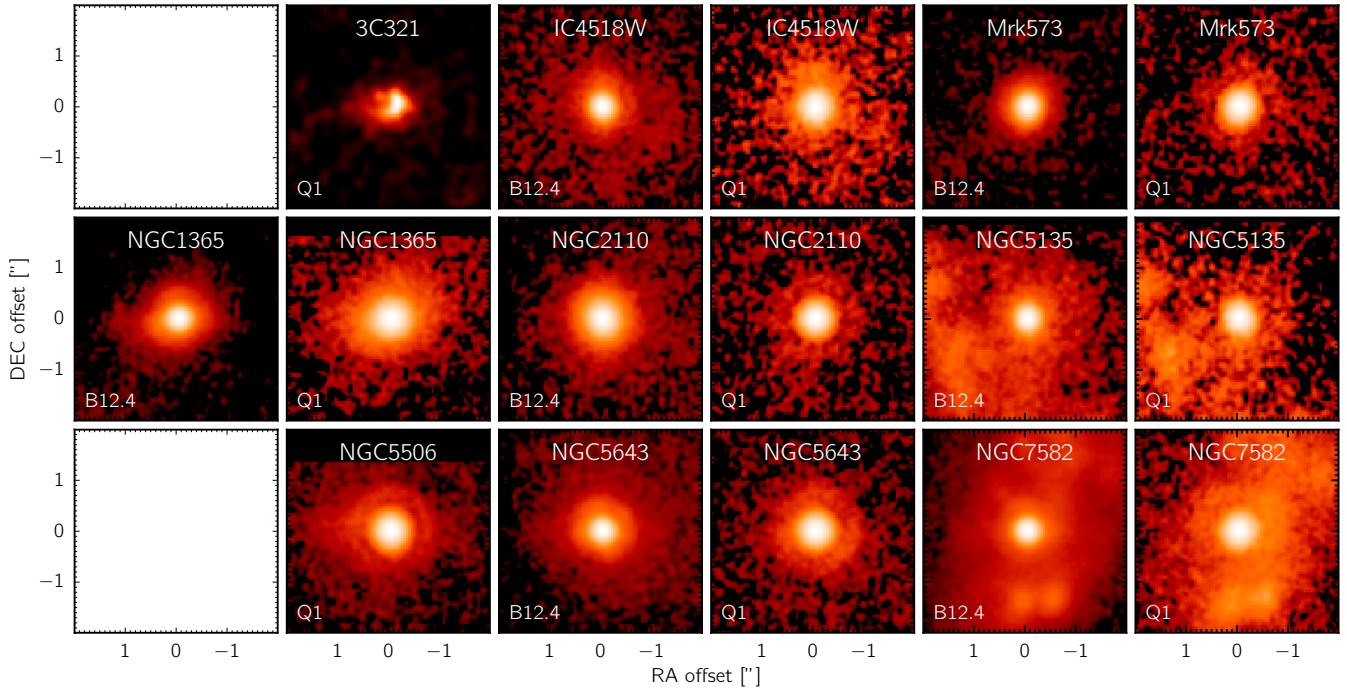


Figure 1. VISIR B12.4 ($12.47 \pm 0.5 \mu\text{m}$) and Q1 ($17.65 \pm 0.44 \mu\text{m}$) images of the central $4'' \times 4''$ region of the observed AGN. The colour scaling is logarithmic in all images except for 3C 321 (where it is linear) with black corresponding to the background level of the image and white to the brightest pixel. All images were slightly smoothed with a Gaussian kernel with $\sigma = 1 \text{ px}$.

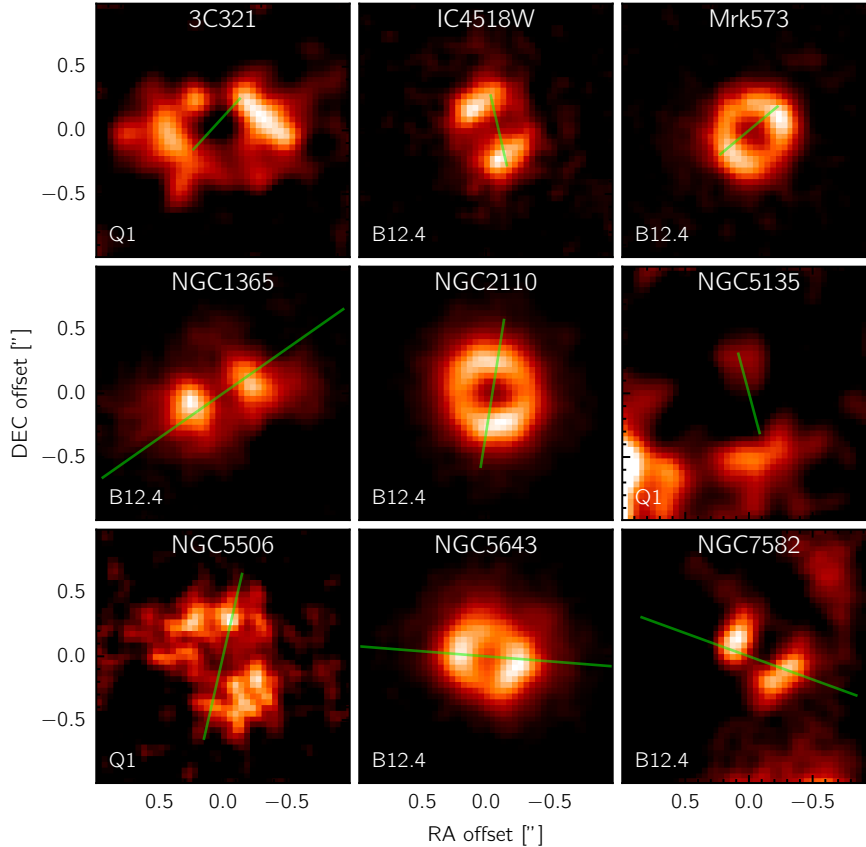


Figure 2. Zoom into the central $2'' \times 2''$ region after deliberately over-subtracting the central point source with the corresponding calibrator star used as PSF reference (see text for details). The best image for each source, either B12.4 ($12.47 \pm 0.5 \mu\text{m}$) or Q1 ($17.65 \pm 0.44 \mu\text{m}$), was selected as explained in the text. The colour scaling is linear in all images with black corresponding to the background level of the image and white to the brightest pixel. All images were slightly smoothed with a Gaussian kernel with $\sigma = 1$ px to increase visibility (2 px for 3C 321 and NGC 5135). The green line in each image marks the system axis PA and has a length of 200 pc at the source distant (except for 3C 321 where it is 1 kpc).

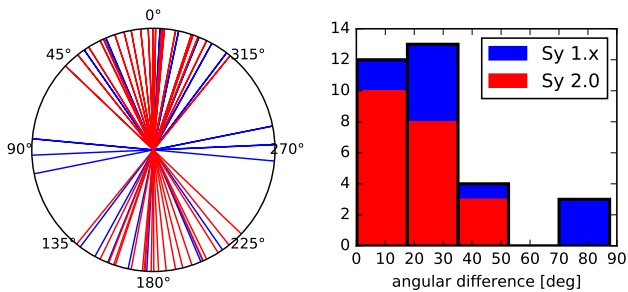


Figure 3. Distribution of the angular difference between the system axis and MIR PAs for all MIR-extended Seyferts from this work and A16 combined. Left: angular plot showing individual objects as lines with Seyfert 1.x (2) in blue (red). Right: Additive histogram of absolute difference with the contribution of the Seyfert 1.x (2) objects is marked in blue (red).

we define as all MIR emission that is caused by AGN heating. In practise, we estimate the latter by integrating all flux within a $2''$ diameter aperture in our VISIR images. This value was chosen as compromise to encompasses as much extended emission as possible but not too much noise. To separate the extended and unresolved emission the accurate PSF references are particularly useful because they allow us to perform a scaled point source subtraction

of the unresolved core. Here we assume the underlying brightness distribution of the extended emission to be flat and thus aim for corresponding point source scaling to obtain a smooth, centrally flat residual (see Sect. 4.3.1 for a discussion of this assumption). Then, the extended emission is estimated as the sum of the residual emission within the $2''$ aperture, and its relative contribution, $R_{\text{AGN}}^{\text{ext}}$, is the ratio of the extended over the total AGN emission.

We find the right scaling by creating a sequence of images with increasing subtraction amplitude. This process is illustrated in Fig. 4 for one source (NGC 5643). The resulting values for $R_{\text{AGN}}^{\text{ext}}$ are listed for all objects in Table 4, while the corresponding sequence plots, can be found in the Appendix (except for 3C 321 where the low S/N of the image does not allow for better estimate than subtracting the point source to 100%). On median, $R_{\text{AGN}}^{\text{ext}}$ is 48% (standard deviation 18%), ranging from 22%, in NGC 5135, to 70%, in NGC 2110.

4.3.1 Robustness of method

This method, despite being somewhat arbitrary and subjective has been commonly used in the literature to separate unresolved and extended components due to the lack of a more objective approach (e.g., Radomski et al. 2002, 2003; Soifer et al. 2003; Ramos Almeida et al. 2009). We will address the possible caveats of this method with some tests. Firstly, we verify that we obtain similar re-

Table 3. Position angles

Object	SA	Ref.	host	Ref.	MIR
	PA		PA		PA
(1)	[deg]	(3)	[deg]	(5)	[deg]
(1)	(2)	(3)	(4)	(5)	(6)
3C 321	138	1, 2	186	3	99
IC 4518W	13	4	-45	3	17
Mrk 573	130	5, 6, 7, 8	180	9	169
NGC 1365	125	10, 11, 12, 13, 14	20	3	102
NGC 2110	-9	15, 16, 17, 18	-5	3	17
NGC 5135	15	19, 20	-60	9	1
NGC 5506	-13	21, 22	89	3	24
NGC 5643	86	23, 24, 25	90	9	67
NGC 7582	70	24, 12	156	3	82

– *Notes:* (1) object name; (2) and (3) system axis position angle and corresponding references based on the NLR major axis from [O III] images, nuclear radio morphology, polarised broad lines, or resolved maser emission (adopted from A16). (4) and (5) host inner structure position angle and corresponding reference (adopted from A16); (6) mean nuclear MIR PA as determined in this work; list of references: 1: Baum et al. (1988); 2: Young et al. (1996); 3: Hyperleđa; 4: Rodríguez-Zaurín et al. (2011); 5: Pogge & De Robertis (1995); 6: Schmitt & Kinney (1996); 7: Ulvestad & Wilson (1984); 8: Nagao et al. (2004); 9: this work; 10: Phillips et al. (1983); 11: Jorsater, Lindblad & Boksenberg (1984); 12: Storchi-Bergmann & Bonatto (1991); 13: Kristen et al. (1997); 14: Sandqvist, Joersaeter & Lindblad (1995); 15: Mulchaey et al. (1994); 16: Ulvestad & Wilson (1983); 17: Nagar et al. (1999); 18: Moran et al. (2007); 19: González Delgado et al. (1998); 20: Ulvestad & Wilson (1989); 21: Colbert et al. (1996); 22: Lumsden, Alexander & Hough (2004); 23: Simpson et al. (1997); 24: Morris et al. (1985); 25: Leipski et al. (2006);

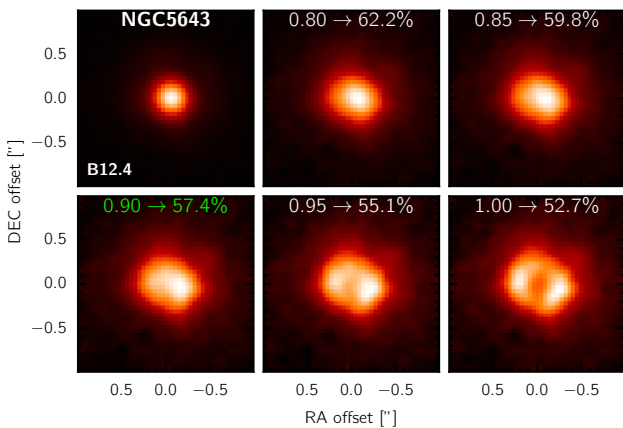


Figure 4. Estimation of extended flux contribution to total AGN flux, $R_{\text{AGN}}^{\text{ext}}$, for NGC 5643 in the B12.4 ($12.47 \pm 0.5 \mu\text{m}$) filter. Shown is the central $2'' \times 2''$ region with similar colour scaling and smoothing to Fig. 2. The top left image shows the original, while the bottom right shows 100% subtraction. The others in between show a sequence of increasing relative amplitude for point source subtraction (the first number in each subplot from left to right). The two numbers in each subplot give the scaling of the point source relative to the emission peak and the resulting contribution of the residual toward the total flux, $R_{\text{AGN}}^{\text{ext}}$, as measured in an $2''$ diameter aperture. The selected scaling is marked in green.

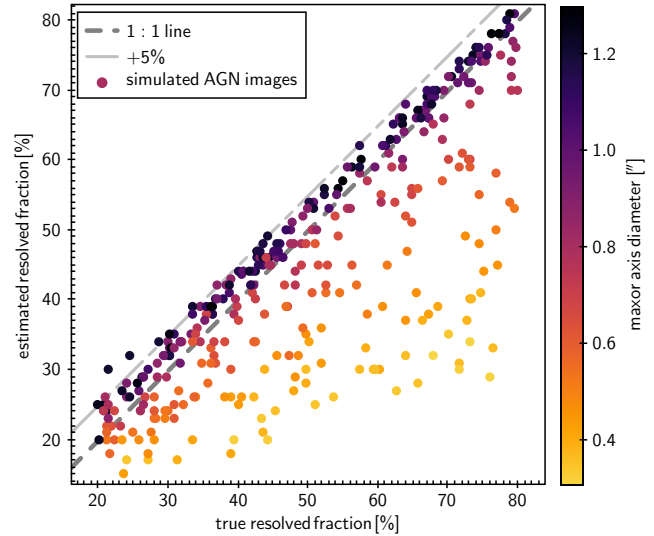


Figure 5. Estimation of extended flux contribution to total flux, $R_{\text{AGN}}^{\text{ext}}$, for 350 simulated images in the B12.4 filter. The random, hidden input $R_{\text{AGN}}^{\text{ext}}$ is shown on the x axis while the estimated value is on the y axis. The symbols are colour coded by the random size of the ellipsoid representing the extended emission. The dot-dashed and dashed line show the 1:1 and the 1:1 +5% relation, respectively. For details, see Sect. 4.3.1.

sults for using the observatory provided standard stars. Using those, the resolved fractions are on average 4.5% smaller but consistent within 1σ (standard deviation is 5%).

Secondly, we subtract our PSF references from the observatory standards to test the amplitude of any artefacts of the subtraction method. The resulting $R_{\text{AGN}}^{\text{ext}}$ measured in the same way as for our AGN, are on average only 5% (standard deviation 11%), so much smaller than our resolved fractions measured for the AGN.

Finally, we test whether there is a systematic bias in our flux estimates owing to the tuning "by eye". For this purpose, we create a simulation where we add a PSF-convolved elliptical extended component with random amplitude, size and orientation to the B12.4 image of NGC 5135. We chose this image because it does not show significant extended emission and matches in terms of S/N to our other AGN images better than any calibrator star observation. Furthermore, the circumnuclear emission in NGC 5135 presents are harder challenge to test our method. The range for the amplitude and size of the ellipsoid are matched to the detected extended emission in our AGN but the exact generated values remain hidden during the test. We then measure the extended flux contribution, $R_{\text{AGN}}^{\text{ext}}$, in the same way as for our real observations and calculate the difference of real value minus estimated value. We repeat this 350 times, at which stage the resulting statistics have converged to $< 1\%$. The resulting distribution of the real and estimated $R_{\text{AGN}}^{\text{ext}}$ is shown in Fig. 5. On average, our method underestimates the true $R_{\text{AGN}}^{\text{ext}}$ by 6% with a standard deviation of 11%. The distribution of difference between true and estimated value is however highly asymmetric: the with 80% of the values lying between -3% and +23%. This asymmetry is caused by the fact that we tend to underestimate the contribution of the extended component if it is compact as shown by the colour coding in Fig. 5. The compacter the extended emission, the more of it is accounted to the point source by our method mistake. On the other hand, the method only rarely overestimates the contribution of the extended component by more than 5% ($< 1\%$ of the cases).

Table 4. Properties of full polar dust AGN sample

Object	Sy	D	$\log L(12\ \mu\text{m})$	$\log L^{\text{int}}(2\text{-}10\ \text{keV})$	$\log N_{\text{H}}$	$\log M_{\text{BH}}$	Ref.	$\log \lambda_{\text{Edd}}$	$R_{\text{AGN}}^{\text{ext}}$	d_{MIR}	d_{MIR}
(1)	(2)	[Mpc]	[erg/s]	[erg/s]	[cm^{-2}]	[M_{\odot}]	(8)	(9)	[%]	[$''$]	[pc]
new (this work)											
3C 321	2.0	460.0	44.6	43.7	24.0	70	1.19	2210
IC 4518W	2.0	76.1	43.5	43.0	23.3	8.8	1	-2.80	48	1.09	389
Mrk 573	2.0	73.1	43.5	43.2	≥ 24.2	6.9	2	-0.81	49	0.89	305
NGC 1365	1.8	17.9	42.5	42.1	23.2	7.3	3	-2.25	46	1.26	109
NGC 2110	2.0	35.9	43.1	42.7	22.5	8.7	3	-3.16	70	1.13	194
NGC 5135	2.0	66.0	43.2	43.2	24.4	7.0	4	-0.85	22	0.83	258
NGC 5506	1.9	31.6	43.4	43.1	22.4	7.6	3	-1.59	32	0.98	148
NGC 5643	2.0	20.9	42.5	42.1	≥ 24.3	7.0	5	-2.00	57	1.06	106
NGC 7582	1.8	23.0	42.9	42.4	23.1	7.7	6	-2.46	44	0.71	79
known (A16)											
Cen A	2.0	3.8	41.8	42.0	23.1	7.7	7	-2.89	26	0.72	13
Circinus	2.0	4.2	42.6	42.3	24.7	6.2	8	-1.07	40	3.00	61
Cygnus A	2.0	257.0	44.1	44.3	23.3	8.8	9	-1.61	60	1.16	1299
ESO 323-77	1.2	71.8	43.7	42.8	23.6	7.4	10	-1.73	43	0.88	297
ESO 428-14	2.0	28.2	42.4	42.6	≥ 24.3	6.8	3	-1.25	68	1.75	236
IC 5063	2.0	49.1	43.8	42.9	23.4	7.8	3	-2.06	58	1.08	251
MCG-03-34-064	2.0	79.3	44.0	43.3	23.6	7.7	11	-1.52	60	1.14	423
NGC 1068	2.0	14.4	43.9	43.6	≥ 25.0	6.9	12	-0.39	75	1.55	108
NGC 1386	2.0	16.5	42.4	42.0	≥ 24.3	7.4	3	-2.54	62	1.30	104
NGC 2992	1.8	39.7	42.9	42.5	22.0	7.4	3	-2.02	30	0.99	187
NGC 3081	2.0	40.9	42.9	42.5	23.9	7.4	4	-1.95	51	2.13	414
NGC 3227	1.5	22.1	42.5	42.1	22.2	6.9	13	-1.85	47	1.02	108
NGC 3281	2.0	52.8	43.6	43.4	24.3	7.4	4	-1.07	40	1.09	273
NGC 4151	1.5	13.3	42.8	42.5	22.7	7.7	14	-2.27	22	1.28	83
NGC 4388	2.0	19.2	42.3	42.3	23.5	6.9	15	-1.76	46	1.02	95
NGC 4593	1.0	45.6	43.1	42.9	20.4	7.0	16	-1.24	34	0.98	212
NGC 5728	2.0	45.4	42.5	42.8	24.1	7.9	17	-2.17	50	0.88	190
NGC 7172	2.0	34.8	42.8	42.8	22.9	7.3	4	-1.62	50	1.19	198
NGC 7314	2.0	18.3	41.8	42.0	22.0	5.5	11	-0.64	54	0.85	75
NGC 7469	1.5	67.9	43.8	43.2	≤ 20.7	7.1	18	-1.00	30	0.82	262
NGC 7674	2.0	126.0	44.3	44.0	≥ 24.4	7.3	3	-0.35	53	1.35	779

– Notes: (1), (2), (3), and (4) object name, optical class, distance (D), and observed nuclear $12\ \mu\text{m}$ continuum luminosity, $L(12\ \mu\text{m})$, from Asmus et al. (2014); (5) and (6) intrinsic 2–10 keV X-ray luminosity, $L^{\text{int}}(2\text{-}10\ \text{keV})$, and obscuring X-ray column density, N_{H} , from Asmus et al. (2015), except NGC 5643 which was taken from Annuar et al. (2015); (7), (8) and (9) estimated black hole mass, M_{BH} , corresponding reference and resulting Eddington ratios, λ_{Edd} , assuming a bolometric luminosity $L_{\text{bol}} = 10L^{\text{int}}(2\text{-}10\ \text{keV})$; (10) resolved fraction of the total nuclear MIR emission as estimated in this work from PSF subtraction; (11) and (12) measured major axis diameters containing 80% of the total AGN MIR emission in angular and absolute units, $d_{\text{MIR}}/''$ and d_{MIR}/pc , respectively; list of references: 1: Koss et al. (2017); 2: Bian & Gu (2007); 3: Hyperleada; 4: Garcia-Rissmann et al. (2005); 5: Beifiori et al. (2009); 6: Wold et al. (2006); 7: Cappellari et al. (2009); 8: Greenhill et al. (2003); 9: Gebhardt et al. (2003); 10: Wang & Zhang (2007); 11: Cid Fernandes et al. (2004); 12: Lodato & Bertin (2003); 13: Denney et al. (2010); 14: Winter et al. (2009); 15: Kuo et al. (2011); 16: Denney et al. (2006); 17: McElroy (1995); 18: Peterson et al. (2004);

Finally, one could question the assumption of the extended emission to have a smooth, flat profile in the central $\sim 0.4''$ region. Firstly, even in the worst case scenario, namely that it actually would have zero emission in the centre, which is the same as the 100% subtraction shown in Fig. 2, we would get only 7% smaller $R_{\text{AGN}}^{\text{ext}}$ on average, thus not changing our conclusions. Secondly, the size of the VISIR PSF would require the underlying brightness distribution to have a “hole” with a projected radius of $> 0.2''$ ($> 40\ \text{pc}$ at the median object distance) to produce a central drop in the PSF-convolved brightness distribution in the observed images. However, such a scenario seems unlikely if the extended dust is part of the AGN structure and is centrally heated, as the previous results indicate. Therefore, we believe our flat profile assumption to be reasonable.

In summary, we conclude that our method is robust to within 10% on average and, if anything, rather underestimates the extended flux for our objects.

4.3.2 Application to full sample

We also employ the same method to similar imaging data of the A16 sample to obtain improved values of $R_{\text{AGN}}^{\text{ext}}$ for all AGN with detected polar dust emission. Details on those data will be presented in a future work (based on ESO programmes 099.B-0235, 100.B-0056, and 101.B-0334; PI Hönic; Asmus et al., in prep.). Furthermore, we add two objects, IC 4329A and NGC 4151, which were discussed in A16 to have good evidence for polar dust emission as well (e.g., Radomski et al. 2003). The resulting distribution

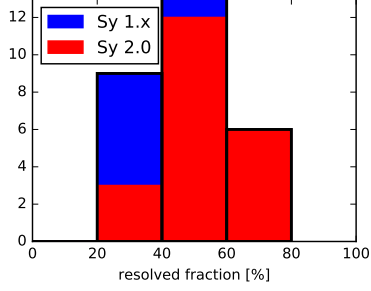


Figure 6. Distribution of minimum relative contribution of the polar extended emission, $R_{\text{AGN}}^{\text{ext}}$, for all MIR-extended Seyferts from this work and A16 combined. The histogram is additive with the contribution of the Seyfert 1.x (2) objects marked in blue (red).

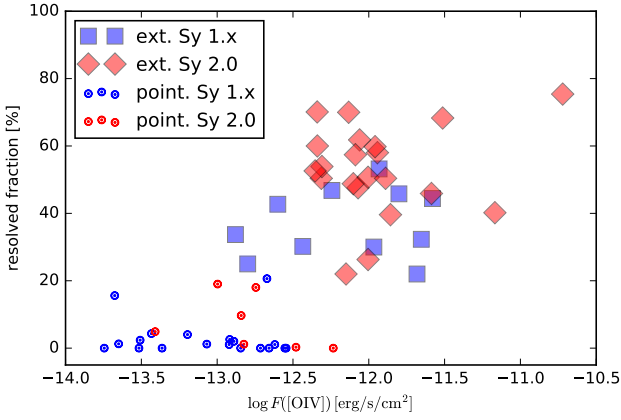


Figure 7. Minimum relative contribution of the polar extended emission, $R_{\text{AGN}}^{\text{ext}}$, over the [OIV] flux, $F([\text{OIV}])$, for all MIR-extended Seyferts from this work and A16 combined. Extended Seyfert 2 objects are marked by red diamonds while extended Seyfert 1.x are blue squares. For comparison, the point-like Seyferts from the total sample of A16 are shown with \odot symbols (blue: Sy 1.x; red: Sy 2).

of $R_{\text{AGN}}^{\text{ext}}$ is shown in Fig. 6. The median value of $R_{\text{AGN}}^{\text{ext}}$ is 49% with a standard deviation of 14%, whereas Seyfert 2 AGN have on average a larger $R_{\text{AGN}}^{\text{ext}}$ than Seyfert 1.x AGN (53% versus 34%). This trend is explained by Seyfert 2s having larger inclinations with respect to our line of sight, leading to larger projected angular sizes of the polar structures.

We also update the found trend of increasing resolved fraction with increasing [OIV] flux, which was used for selecting the sample (Fig. 7). The significance of this trend increases slightly with adding the new sources, i.e., the null hypothesis probability of the corresponding Spearman rank test drops from $3 \cdot 10^{-7}$ to $6 \cdot 10^{-9}$ while the rank increases slightly from 0.66 to 0.68.

We emphasize that $R_{\text{AGN}}^{\text{ext}}$ only provides a lower limit for the actual contribution of the polar dust emission, $R_{\text{AGN}}^{\text{pol}}$, because a large part of the latter remains unresolved with VISIR. This is obvious from the VLTI/MIDI results that show prominent polar extended MIR emission at an order of magnitude higher angular resolution in all objects with sufficient u,v coverage (López-Gonzaga et al. 2016). In general, the polar dust emission turns out to be the dominating component on these scales with an median flux contribution of $R_{\text{MIDI}}^{\text{pol}} = 67 \pm 13\%$. Now, the VISIR unresolved component corresponds to the total flux as seen MIDI, i.e., the value at baseline length 0 (see e.g., Burtscher et al. 2013 for de-

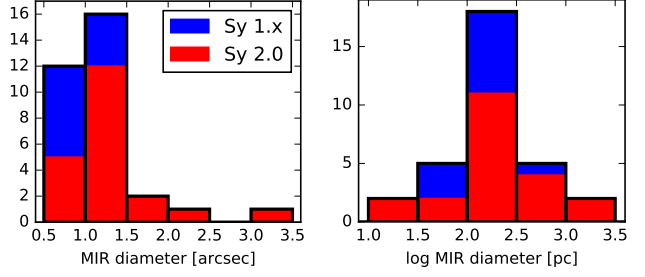


Figure 8. Distribution of the MIR major axis diameters containing 80% of the total nuclear flux, d_{MIR} , for all MIR-extended Seyferts from this work and A16 combined. The contributions of the Seyfert 1.x (2) are marked in blue (red). Left: sizes are in angular units. Right: size are in absolute units.

tails). Therefore, the actual contribution of the polar dust emission is given by the combination of the resolved fraction in VISIR and the polar component contribution in MIDI, i.e., $R_{\text{AGN}}^{\text{pol}}/[\%] = R_{\text{AGN}}^{\text{ext}} + (100 - R_{\text{AGN}}^{\text{ext}})(R_{\text{MIDI}}^{\text{pol}}/100)$, which is 83% for the median values above. This implies the polar dust on average dominates the total MIR emission of AGN.

Here, we do not explicitly take into account obscuration effects in the mid-infrared. For example, Stalevski et al. (2016) find that self-shielding of clumpy dust distributions around AGN can cause a factor ~ 2 decrease of the observed $12 \mu\text{m}$ emission for close to edge-on sight lines. However, such hiding of obscuring dust emission would occur only on parsec-scales, so affect only MIDI measurements. Therefore, even if the parsec-scale component would be intrinsically brighter by a factor of two, the median of $R_{\text{MIDI}}^{\text{pol}}$ would become 51% for the values from López-Gonzaga et al. (2016), i.e., the MIR emission would still be dominated by the polar dust.

4.4 Extent of polar dust emission

In this section, we investigate the extent of the polar dust structures. Despite the relatively long exposure times of the new VISIR images presented here (30 min on source), the detection of the extended MIR structures is still limited by low signal-to-noise ratios. This is because ground-based MIR instruments have a relatively poor sensitivity for extended emission owing to the background noise increasing with the diameter of the telescope at the same rate as the collected photons from the source. Thus, the full extent of the polar dust emission can only be probed from space, i.e., with the *James Webb Space Telescope* (JWST; Gardner et al. 2006). However, we can at least derive lower limits on the former with the VISIR images. For this purpose, we measure the extent of the region which contains 80% of the total nuclear emission by masking the rest and fitting an ellipse. This threshold was chosen in analogy to the FWHM of a Gaussian and should roughly account for the PSF-widening under the assumption that the surface brightness of the polar dust drops smoothly. We use the major axis diameter of the fitted ellipse, d_{MIR} , as measure for the MIR size. Note that this method gives larger sizes than the major axis FWHM values of the previous Gauss fits because the latter is usually dominated by the unresolved core and, thus, misses a significant part of the extended emission.

The distribution of d_{MIR} for all polar extended AGN is shown in Fig. 8, while the individual values are listed in Table 4. As explained above, the relatively poor sensitivity for extended emission leads to the resulting angular sizes falling into a narrow range for

most objects, namely $d_{\text{MIR}} \sim 1.1'' \pm 0.3''$. Converted into absolute units at the object distance, D , d_{MIR} ranges from 13 pc in Cen A to 2.2 kpc in 3C 321 with a median of 198 pc (standard deviation 418 pc; right side of Fig. 8). While the absolute sizes are more physical meaningful for the investigation of any trends of the polar MIR emission size with other AGN parameters, we need to keep in mind that the d_{MIR}/pc are still lower limits that, owing to the above caveat, are dominated by the object distance, i.e., d_{MIR}/pc and D are strongly correlated.

4.5 Dependence on AGN-fundamental parameters

As already mentioned, the most likely explanation for significant amount of dust in the polar region of the AGN is a roughly vertically launched dusty wind driven by radiation from the accretion disk. In this scenario, it is naturally expected that the amount of dust and the size of the outflow will be connected with the AGN-fundamental parameters of luminosity and/or accretion rate. Therefore, we test for any empirical correlations of our derived lower limits for the contribution and size of the polar dust emission, $R_{\text{AGN}}^{\text{ext}}$ and d_{MIR} , with the bolometric luminosity, L_{bol} and the Eddington ratio, λ_{Edd} . Here, L_{bol} is approximated simply as $L_{\text{bol}} = 10L^{\text{int}}(2-10 \text{ keV})$, following, e.g., Vasudevan & Fabian (2007) and Vasudevan et al. (2009) with $L^{\text{int}}(2-10 \text{ keV})$ the intrinsic 2-10 keV X-ray luminosity, while $\lambda_{\text{Edd}} = L_{\text{bol}}/L_{\text{Edd}}$ with $\lambda_{\text{Edd}} = 1.26 \cdot 10^{38} (M_{\text{BH}}/M_{\odot}) \text{ erg/s}$ the Eddington luminosity and M_{BH} the black hole mass. The values for $L^{\text{int}}(2-10 \text{ keV})$ and M_{BH} are collected from the literature and are listed in Table 4.

We tested for correlations between all the above quantities, expressing d_{MIR} in angular, absolute and relative units. For the latter, we express d_{MIR} in units of the sublimation radius, r_{sub} , which is approximated as $r_{\text{sub}} = 0.47 \sqrt{L_{\text{bol}}/10^{46} \text{ erg s}^{-1}} \text{ pc}$, under the assumption that the innermost dust is dominated by graphite grains of 0.04 μm size with a sublimation temperature of 1500 K (Kishimoto et al. 2007).

Unfortunately, our sample spans only a narrow range in luminosity for a given distance, leading to artificially strong correlations whenever distance and luminosity are involved. Once this caveat is taken into account, no statistically significant correlations remain. This does not mean that there are no intrinsic correlations between, e.g., L_{bol} and $R_{\text{AGN}}^{\text{ext}}$ or d_{MIR} but they remain hidden by the dominating distance effects in our sample.

That being said, a possible correlation between d_{MIR}/pc and the Eddington ratio is found (Fig. 9). It can be represented by a linear relation in logarithmic space with a slope of $\sim 0.29 \pm 0.15$ according to a fit using the ordinary least squares method with λ_{Edd} as independent variable. Here, the uncertainties are dominated by the black hole mass estimates which were collected from different methods but often with uncertainties of the order of 0.4 dex. We quantify the significance of this relation using the Kendall's Tau which is $\tau_{\text{K}} = 0.3$ with a null hypothesis probability of $p_{\text{K}} = 0.018$. While this is usually not regarded as formally significant, we note the following features in support of the correlation being real. First, the correlation properties do not change if we use the [OIV] luminosity to estimate L_{bol} instead of the X-ray luminosity. Second, the correlation of D with λ_{Edd} is weaker, although just slightly ($\tau_{\text{K}} = 0.28$ and $p_{\text{K}} = 0.03$). A correlation of the Eddington ratio with the distance would also be surprising owing to the distance cancelling out in the luminosity ratio used to calculate λ_{Edd} . And third and somewhat surprising, the correlation is stronger for the Seyfert 1.x only ($\tau_{\text{K}} = 0.78$ and $\log p_{\text{K}} = -3.1$).

The latter finding is quite puzzling because the Seyfert 1.x

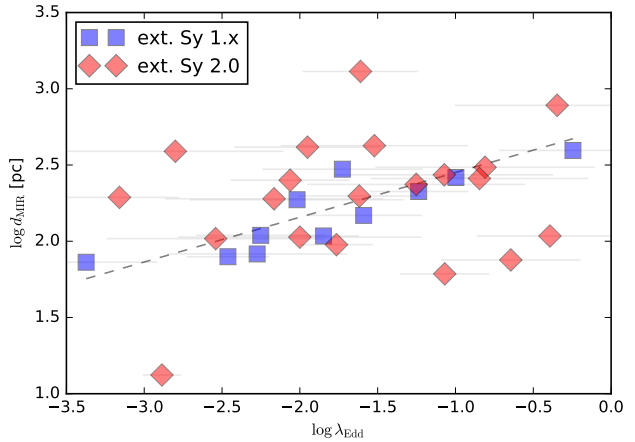


Figure 9. MIR diameter, d_{MIR}/pc versus Eddington ratio, λ_{Edd} , in logarithmic space for all MIR-extended Seyferts from this work and A16 combined. Extended Seyfert 2 objects are marked by red diamonds while extended Seyfert 1.x are blue squares. The linear fit described in the main text is shown as black dashed line.

sources are expected to be seen rather face-on leading to smaller and less reliable projected sizes. As said, there is a strong correlation of d_{MIR}/pc with D but it is in fact weaker for the Seyfert 1.x than for the Seyfert 2, which disfavors a distance effect being at work here. Next, one might expect a correlation of the black hole mass with the distance because the estimation methods for M_{BH} might depend on intrinsic resolution. However, there is no such correlation present in our data, in particular for the Seyfert 1.x. On the other hand, we note that the Eddington ratio is much more uncertain for the Seyfert 2s because both the black hole mass and bolometric luminosity estimates are less reliable, owing to being indirect and absorption correction dependent, respectively. This could explain the larger scatter of the Seyfert 2s, masking any correlation for them.

Certainly, the found trend of increasing absolute MIR size with Eddington ratio should be regarded with a lot of caution. It is unexpected and based on few objects and at the limit of what can be done with the VISIR data. However, we failed to identify any artificial cause for such a correlation. If it would prove to be true, then it would indicate a new relation of the polar dust structure with an AGN fundamental parameter that might provide important constraints for the modelling and thus further understanding of the polar emission and its underlying physics. Therefore, we discuss its implications a bit further below.

Naively, one would expect that the size of the polar MIR emitting structure scales with the luminosity. This would then imply the Eddington ratio to correlate with $d_{\text{MIR}}/r_{\text{sub}}$ rather than d_{MIR}/pc , as found. However, as said, our dataset does not allow us to isolate any such correlation. At least for the less-inclined Seyfert 1.x, a possible explanation for the found correlation could be a widening of the opening angle with increasing Eddington ratio, leading to larger projected diameters. Related to that, Ezhikode et al. (2017) found a decrease in the dust covering factor, i.e., the ratio of the infrared to bolometric luminosity, with increasing Eddington ratio. They also found that this trend is stronger with λ_{Edd} than with L_{bol} . Similar results were obtained for the nuclear obscuration seen in X-rays (Fabian, Vasudevan & Gandhi 2008; Fabian et al. 2009; Ricci et al. 2017). In particular in the latter work, a deficit of obscured systems at high Eddington ratios could be shown, implying that the radia-

tion pressure of the AGN becomes so strong at high λ_{Edd} that the non-equatorial regions are cleared from obscuring material. Both results imply an increase in the opening angle of the dusty outflow, which might also explain our finding. On the other hand, an increase of the opening angle would imply a decrease of the MIR–X-ray emission ratio with increasing λ_{Edd} , which we do not see in our sample. Alternatively, the larger MIR diameter for larger Eddington ratios might be caused by material blown to larger scales. Detailed modelling of the dust structure in the polar dust AGN might allow us to further distinguish between the above scenarios but is beyond the scope of this work.

5 SUMMARY & CONCLUSIONS

We have observed 9 nearby, obscured Seyfert-type AGN with deep subarcsecond resolution MIR images to look for polar dust emission, which was predicted to be present in all of them given by their [OIV] brightness and inclination. Extended emission was detected in 8 out of 9 cases at more than 3σ , and in the remaining case at $\sim 2\sigma$ level. We showed that this extended MIR emission is aligned with the system axis of the AGN in projection. Thus, the above prediction was confirmed, with the most likely origin of the extended MIR emission being the proposed polar dusty wind. This result suggests that polar dust might be an ubiquitous feature of the AGN structure in general, at least for the probed regime of luminosities and Eddington ratios, which extends over the full Seyfert regime ($42 \lesssim \log L_{\text{bol}} \lesssim 45$ and $-3 \lesssim \log \lambda_{\text{Edd}} \lesssim 0$).

Furthermore, the analyses of the combined samples of all AGN with detected polar dust emission verifies that the majority of the total MIR radiation produced by the AGN is originating from these polar regions. Owing to the polar dust being on similar scales as the NLR, encompassing it at least partly, it has to be optically thin on average to allow us to see the NLR in inclined AGN. As a consequence, the MIR emission should be quite isotropic. This would then explain, among other observations, the similarity of the MIR–X-ray emission ratio of unobscured and obscured AGN as found in the form of a tight MIR–X-ray luminosity relation (e.g., Gandhi et al. 2009; Asmus et al. 2015; Mateos et al. 2015). Furthermore, it would cast doubt on parameters derived from spectral energy distribution fitting in the infrared with clumpy torus models, in particular the covering factor of optically thick material.

In other words, the MIR is probably not tracing the main obscuring structure in AGN. It might not even trace the bulk of the dusty material, which may reside in the much cooler structures that are shielded from the direct AGN emission and now are resolved with ALMA in several nearby AGN (García-Burillo et al. 2014, 2016; Gallimore et al. 2016; Izumi et al. 2018; Alonso-Herrero et al. 2018; Combes et al. 2019).

Finally, we found a tentative trend of increasing size of the polar MIR emitting region with increasing Eddington ratio which is significant at least for Seyfert 1.x AGN. While we caution of an unidentified artificial origin, one possible physical explanation would be a widening of the opening angle of the dusty outflow with increasing λ_{Edd} .

To better understand the dust structure in AGN, detailed modelling will be required. Here, as demonstrated in Stalevski, Asmus & Tristram (2017) and Stalevski, Tristram & Asmus (2019), taking into account the spatial information when comparing data to models is absolutely critical to break the degeneracies that occur if one only fits the integrated spectral energy distributions. Therefore, we plan to test both the polar dust cone and clumpy torus scenarios

for the whole polar dust AGN sample in a follow-up work, where we will use the most recent radiative transfer models by Hönig & Kishimoto (2017) and Stalevski, Asmus & Tristram (2017) to perform a combined fitting of the spectral and spatial properties of the sample (Asmus et al., in prep.).

Eventually, *JWST* will enable us significantly advance on the results presented here thanks to its vastly better sensitivity to extended emission, allowing for larger samples and more accurate size estimates at the same time.

ACKNOWLEDGEMENTS

DA thanks the anonymous referee for critical but constructive comments that helped to a more balanced discussion. DA as well thanks M. Kishimoto, M. Stalevski and K.R.W. Tristram for very helpful and constructive comments on the manuscript, and S.F. Hönig, P. Gandhi, and C. Ricci for their support and feedback at various stages of this work. Furthermore, DA thanks the NED team for providing the table with all the [OIV] measurements included in NED. Based on European Southern Observatory (ESO) observing programme 099.B-0044. DA acknowledges funding through the European Unions Horizon 2020 and Innovation programme under the Marie Skłodowska-Curie grant agreement no. 793499 (DUSTDEV-ILS). This research made use of the NASA/IPAC Extragalactic Database (NED), which is operated by the Jet Propulsion Laboratory, California Institute of Technology, under contract with the National Aeronautics and Space Administration. This research made use of Astropy, a community-developed core Python package for Astronomy (Astropy Collaboration et al. 2013). This research has made use of NASA’s Astrophysics Data System.

REFERENCES

- Almeida C. R., Ricci C., 2017, *Nature Astronomy*, 1, 679
- Alonso-Herrero A. et al., 2018, *ApJ*, 859, 144
- Alonso-Herrero A. et al., 2011, *ApJ*, 736, 82
- Annunzio A. et al., 2015, *ApJ*, 815, 36
- Antonucci R., 1993, *ARA&A*, 31, 473
- Asmus D., Gandhi P., Hönig S. F., Smette A., Duschl W. J., 2015, *MNRAS*, 454, 766
- Asmus D., Hönig S. F., Gandhi P., 2016, *ApJ*, 822, 109
- Asmus D., Hönig S. F., Gandhi P., Smette A., Duschl W. J., 2014, *MNRAS*, 439, 1648
- Astropy Collaboration et al., 2013, *A&A*, 558, A33
- Baskin A., Laor A., 2018, *MNRAS*, 474, 1970
- Baum S. A., Heckman T. M., Bridle A., van Breugel W. J. M., Miley G. K., 1988, *ApJSS*, 68, 643
- Beifiori A., Sarzi M., Corsini E. M., Dalla Bont E., Pizzella A., Coccato L., Bertola F., 2009, *ApJ*, 692, 856
- Bian W., Gu Q., 2007, *ApJ*, 657, 159
- Bock J. J. et al., 2000, *AJ*, 120, 2904
- Burtscher L. et al., 2013, *A&A*, 558, 149
- Cao T. et al., 2018, *ApJ*, 866, 117
- Cappellari M., Neumayer N., Reunanen J., van der Werf P. P., de Zeeuw P. T., Rix H.-W., 2009, *MNRAS*, 394, 660
- Chan C.-H., Krolik J. H., 2016, *ApJ*, 825, 67
- Cid Fernandes R., Gu Q., Melnick J., Terlevich E., Terlevich R., Kunth D., Rodrigues Lacerda R., Joguet B., 2004, *MNRAS*, 355, 273

- Cohen M., Walker R. G., Carter B., Hammersley P., Kidger M., Noguchi K., 1999, *AJ*, 117, 1864
- Colbert E. J. M., Baum S. A., Gallimore J. F., O’Dea C. P., Lehnert M. D., Tsvetanov Z. I., Mulchaey J. S., Caganoff S., 1996, *ApJSS*, 105, 75
- Combes F. et al., 2019, *A&A*, 623, A79
- Denney K. D. et al., 2006, *ApJ*, 653, 152
- Denney K. D. et al., 2010, *ApJ*, 721, 715
- Diamond-Stanic A. M., Rieke G. H., Rigby J. R., 2009, *ApJ*, 698, 623
- Dicken D. et al., 2014, *ApJ*, 788, 98
- Elitzur M., Shlosman I., 2006, *ApJ*, 648, L101
- Elvis M., 2000, *ApJ*, 545, 63
- Ezhikode S. H., Gandhi P., Done C., Ward M., Dewangan G. C., Misra R., Philip N. S., 2017, *MNRAS*, 472, 3492
- Fabian A. C., Vasudevan R. V., Gandhi P., 2008, *MNRAS*, 385, L43
- Fabian A. C., Vasudevan R. V., Mushotzky R. F., Winter L. M., Reynolds C. S., 2009, *MNRAS*, 394, L89
- Fischer T. C., Crenshaw D. M., Kraemer S. B., Schmitt H. R., 2013, *ApJSS*, 209, 1
- Fuller L. et al., 2019, *MNRAS*, 483, 3404
- Gallimore J. F. et al., 2016, *ApJ*, 829, L7
- Gandhi P., Horst H., Smette A., Hönic S., Comastri A., Gilli R., Vignali C., Duschl W., 2009, *A&A*, 502, 457
- García-Burillo S. et al., 2016, *ApJ*, 823, L12
- García-Burillo S. et al., 2014, *A&A*, 567, A125
- García-Rissmann A., Vega L. R., Asari N. V., Cid Fernandes R., Schmitt H., González Delgado R. M., Storchi-Bergmann T., 2005, *MNRAS*, 359, 765
- Gardner J. P. et al., 2006, *Space Science Reviews*, 123, 485
- Gebhardt K. et al., 2003, *ApJ*, 583, 92
- González Delgado R. M., Heckman T., Leitherer C., Meurer G., Krolik J., Wilson A. S., Kinney A., Koratkar A., 1998, *ApJ*, 505, 174
- Greenhill L. J. et al., 2003, *ApJ*, 590, 162
- Günthardt G. I., Agüero M. P., Camperi J. A., Díaz R. J., Gomez P. L., Bosch G., Schirmer M., 2015, *AJ*, 150, 139
- Hönig S. F., Kishimoto M., 2017, *The ApJL*, 838, L20
- Hönig S. F., Kishimoto M., Antonucci R., Marconi A., Prieto M. A., Tristram K., Weigelt G., 2012, *ApJ*, 755, 149
- Hönig S. F. et al., 2013, *ApJ*, 771, 87
- Izumi T., Wada K., Fukushige R., Hamamura S., Kohno K., 2018, *ApJ*, 867, 48
- Jorsater S., Lindblad P. O., Boksenberg A., 1984, *A&A*, 140, 288
- Käuffl H. U. et al., 2015, *The Messenger*, 159, 15
- Kerber F. et al., 2016, in *Society of Photo-Optical Instrumentation Engineers (SPIE) Conference Series*, Vol. 9908, p. 99080D
- Kessler M. F. et al., 1996, *A&A*, 315, L27
- Kishimoto M., Hönig S. F., Beckert T., Weigelt G., 2007, *A&A*, 476, 713
- Konigl A., Kartje J. F., 1994, *ApJ*, 434, 446
- Koss M. et al., 2017, *ApJ*, 850, 74
- Kristen H., Jorsater S., Lindblad P. O., Boksenberg A., 1997, *A&A*, 328, 483
- Kuo C. Y. et al., 2011, *ApJ*, 727, 20
- Lagage P. O. et al., 2004, *The Messenger*, 117, 12
- Leftley J. H., Tristram K. R. W., Hönig S. F., Kishimoto M., Asmus D., Gandhi P., 2018, *ApJ*, 862, 17
- Leipski C., Falcke H., Bennert N., Hüttemeister S., 2006, *A&A*, 455, 161
- Lodato G., Bertin G., 2003, *A&A*, 398, 517
- López-Gonzaga N., Burtscher L., Tristram K. R. W., Meisenheimer K., Schartmann M., 2016, *A&A*, 591, A47
- López-Gonzaga N., Jaffe W., Burtscher L., Tristram K. R. W., Meisenheimer K., 2014, *A&A*, 565, A71
- Lumsden S. L., Alexander D. M., Hough J. H., 2004, *MNRAS*, 348, 1451
- Mateos S. et al., 2015, *MNRAS*, 449, 1422
- McElroy D. B., 1995, *ApJSS*, 100, 105
- Meléndez M. et al., 2008, *ApJ*, 682, 94
- Moran E. C., Barth A. J., Eracleous M., Kay L. E., 2007, *The ApJL*, 668, L31
- Morris S., Ward M., Whittle M., Wilson A. S., Taylor K., 1985, *MNRAS*, 216, 193
- Mulchaey J. S., Wilson A. S., Bower G. A., Heckman T. M., Krolik J. H., Miley G. K., 1994, *ApJ*, 433, 625
- Nagao T., Kawabata K. S., Murayama T., Ohyama Y., Taniguchi Y., Sumiya R., Sasaki S. S., 2004, *AJ*, 128, 109
- Nagar N. M., Wilson A. S., Mulchaey J. S., Gallimore J. F., 1999, *ApJSS*, 120, 209
- Neenkova M., Sirocky M. M., Ivezić v., Elitzur M., 2008, *ApJ*, 685, 147
- Netzer H., 2015, *ARA&A*, 53, 365
- Packham C., Radomski J. T., Roche P. F., Aitken D. K., Perlman E., Alonso-Herrero A., Colina L., Telesco C. M., 2005, *The ApJL*, 618, L17
- Pereira-Santaella M., Diamond-Stanic A. M., Alonso-Herrero A., Rieke G. H., 2010, *ApJ*, 725, 2270
- Peterson B. M. et al., 2004, *ApJ*, 613, 682
- Phillips M. M., Edmunds M. G., Pagel B. E. J., Turtle A. J., 1983, *MNRAS*, 203, 759
- Pier E. A., Krolik J. H., 1992, *The ApJL*, 399, L23
- Pogge R. W., De Robertis M. M., 1995, *ApJ*, 451, 585
- Radomski J. T., Pia R. K., Packham C., Telesco C. M., De Buizer J. M., Fisher R. S., Robinson A., 2003, *ApJ*, 587, 117
- Radomski J. T., Pia R. K., Packham C., Telesco C. M., Tadhunter C. N., 2002, *ApJ*, 566, 675
- Ramos Almeida C. et al., 2011, *ApJ*, 731, 92
- Ramos Almeida C. et al., 2009, *ApJ*, 702, 1127
- Ricci C. et al., 2017, *Nature*, 549, 488
- Rodríguez-Zaurín J., Arribas S., Monreal-Ibero A., Colina L., Alonso-Herrero A., Alfonso-Garzón J., 2011, *A&A*, 527, 60
- Roth N., Kasen D., Hopkins P. F., Quataert E., 2012, *ApJ*, 759, 36
- Sandqvist A., Joersaeter S., Lindblad P. O., 1995, *A&A*, 295, 585
- Schmitt H. R., Kinney A. L., 1996, *ApJ*, 463, 498
- Simpson C., Wilson A. S., Bower G., Heckman T. M., Krolik J. H., Miley G. K., 1997, *ApJ*, 474, 121
- Soifer B. T., Bock J. J., Marsh K., Neugebauer G., Matthews K., Egami E., Armus L., 2003, *AJ*, 126, 143
- Stalevski M., Asmus D., Tristram K. R. W., 2017, *MNRAS*, 472, 3854
- Stalevski M., Ricci C., Ueda Y., Lira P., Fritz J., Baes M., 2016, *MNRAS*, 458, 2288
- Stalevski M., Tristram K. R. W., Asmus D., 2019, *MNRAS*, 484, 3334
- Storchi-Bergmann T., Bonatto C. J., 1991, *MNRAS*, 250, 138
- Sturm E., Lutz D., Verma A., Netzer H., Sternberg A., Moorwood A. F. M., Oliva E., Genzel R., 2002, *A&A*, 393, 821
- Tommasin S., Spinoglio L., Malkan M. A., Fazio G., 2010, *ApJ*, 709, 1257
- Tristram K. R. W., Burtscher L., Jaffe W., Meisenheimer K., Hönig S. F., Kishimoto M., Schartmann M., Weigelt G., 2014, *A&A*, 563, 82

- Ulvestad J. S., Wilson A. S., 1983, *The ApJL*, 264, L7
Ulvestad J. S., Wilson A. S., 1984, *ApJ*, 285, 439
Ulvestad J. S., Wilson A. S., 1989, *ApJ*, 343, 659
Vasudevan R. V., Fabian A. C., 2007, *MNRAS*, 381, 1235
Vasudevan R. V., Mushotzky R. F., Winter L. M., Fabian A. C.,
2009, *MNRAS*, 399, 1553
Vollmer B., Schartmann M., Burtscher L., Marin F., Hönig S.,
Davies R., Goosmann R., 2018, *A&A*, 615, A164
Wada K., 2012, *ApJ*, 758, 66
Wada K., Schartmann M., Meijerink R., 2016, *ApJ*, 828, L19
Wang J.-M., Zhang E.-P., 2007, *ApJ*, 660, 1072
Weaver K. A. et al., 2010, *ApJ*, 716, 1151
Werner M. W. et al., 2004, *ApJSS*, 154, 1
Williamson D., Hönig S., Venanzi M., 2019, *ApJ*, 876, 137
Winter L. M., Mushotzky R. F., Reynolds C. S., Tueller J., 2009,
ApJ, 690, 1322
Wold M., Lacy M., Käuffl H. U., Siebenmorgen R., 2006, *A&A*,
460, 449
Young S., Hough J. H., Efstathiou A., Wills B. J., Axon D. J.,
Bailey J. A., Ward M. J., 1996, *MNRAS*, 279, L72

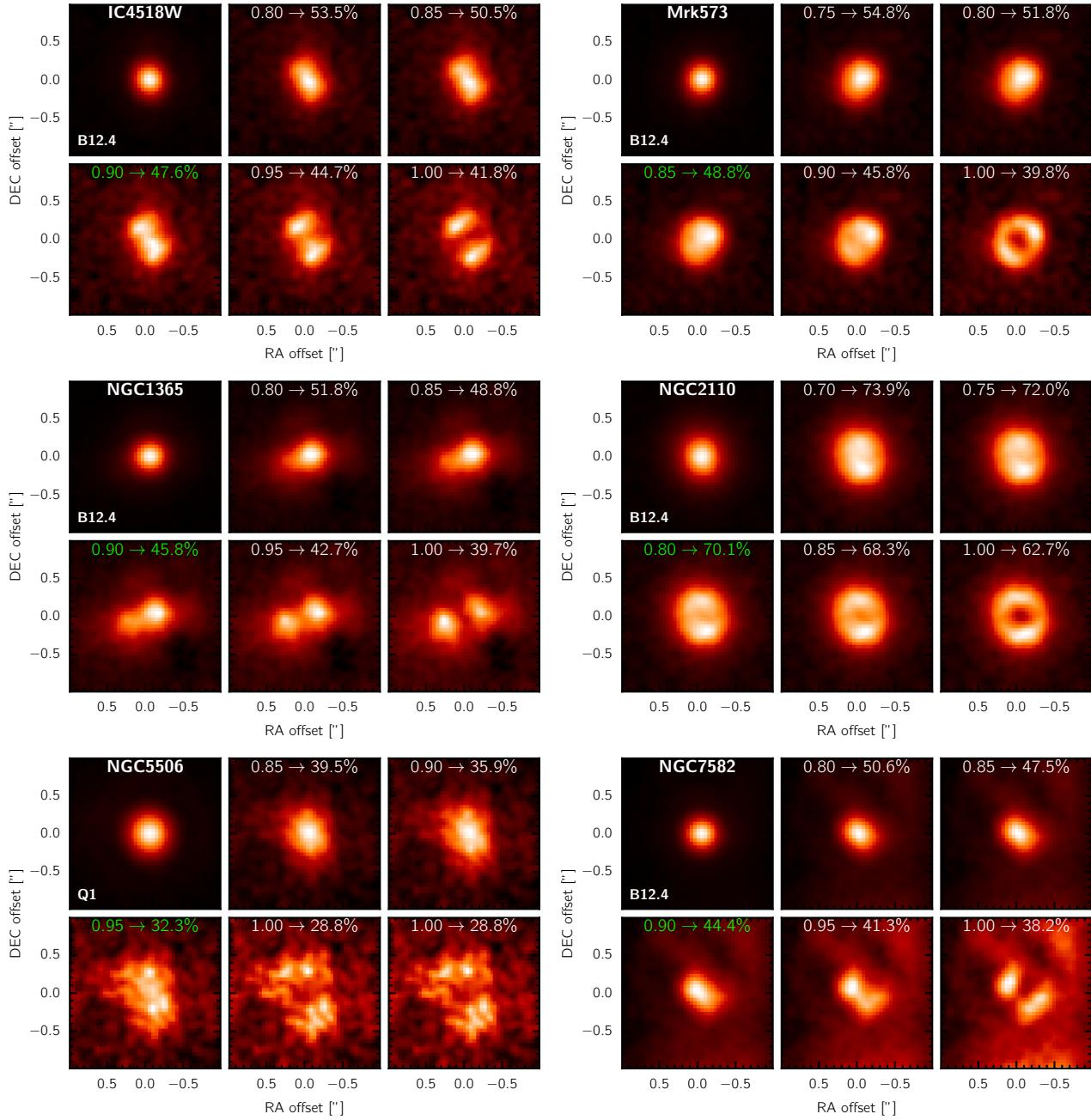


Figure 1. Same as Fig. 4 but for the other objects from the sample, except 3C 321 and NGC 5135.